



## RESEARCH ARTICLE

10.1029/2022AV000800

**Peer Review** The peer review history for this article is available as a PDF in the Supporting Information.

## Key Points:

- The cross-density mixing of water and tracers is quantified from observation-based estimates and numerical simulations in the Atlantic Ocean
- A net 0.5–8 Sv of North Atlantic Deep Water upwells diapycnally in the Atlantic Ocean (48°N–32°S), comprised of larger regional up/downwelling fluxes
- Tracer mixing in the deep Atlantic Ocean can significantly modify pathways and ventilation rates of tracers upwelling in the Southern Ocean

## Supporting Information:

Supporting Information may be found in the online version of this article.

## Correspondence to:

L. Cimoli,  
laura.cimoli@damtp.cam.ac.uk

## Citation:

Cimoli, L., Mashayek, A., Johnson, H. L., Marshall, D. P., Naveira Garabato, A. C., Whalen, C. B., et al. (2023). Significance of diapycnal mixing within the Atlantic meridional overturning circulation. *AGU Advances*, 4, e2022AV000800. <https://doi.org/10.1029/2022AV000800>

Received 22 AUG 2022

Accepted 6 DEC 2022

## Author Contributions:

**Conceptualization:** Laura Cimoli, Ali Mashayek

**Data curation:** Caitlin B. Whalen, Clément Vic, Casimir de Lavergne

**Formal analysis:** Laura Cimoli, Ali Mashayek, Helen L. Johnson, David P. Marshall, Alberto C. Naveira Garabato, Lynne D. Talley

© 2023. The Authors.

This is an open access article under the terms of the [Creative Commons Attribution License](#), which permits use, distribution and reproduction in any medium, provided the original work is properly cited.

## Significance of Diapycnal Mixing Within the Atlantic Meridional Overturning Circulation

Laura Cimoli<sup>1,2,3</sup> , Ali Mashayek<sup>4</sup> , Helen L. Johnson<sup>5</sup> , David P. Marshall<sup>3</sup> , Alberto C. Naveira Garabato<sup>6</sup> , Caitlin B. Whalen<sup>7</sup> , Clément Vic<sup>8</sup> , Casimir de Lavergne<sup>9</sup> , Matthew H. Alford<sup>2</sup> , Jennifer A. MacKinnon<sup>2</sup> , and Lynne D. Talley<sup>2</sup>

<sup>1</sup>Department of Applied Mathematics and Theoretical Physics, University of Cambridge, Cambridge, UK, <sup>2</sup>Scripps Institution of Oceanography, University of California San Diego, La Jolla, CA, USA, <sup>3</sup>Department of Physics, University of Oxford, Oxford, UK, <sup>4</sup>Department of Earth Sciences, University of Cambridge, Cambridge, UK, <sup>5</sup>Department of Earth Sciences, University of Oxford, Oxford, UK, <sup>6</sup>School of Ocean and Earth Science, University of Southampton, Southampton, UK, <sup>7</sup>Applied Physics Laboratory, University of Washington, Seattle, WA, USA, <sup>8</sup>Laboratoire d'Océanographie Physique et Spatiale, University of Brest, CNRS, IRD, Ifremer, Plouzané, France, <sup>9</sup>LOCEAN Laboratory, Sorbonne Université-CNRS-IRD-MNHN, Paris, France

**Abstract** Diapycnal mixing shapes the distribution of climatically important tracers, such as heat and carbon, as these are carried by dense water masses in the ocean interior. Here, we analyze a suite of observation-based estimates of diapycnal mixing to assess its role within the Atlantic Meridional Overturning Circulation (AMOC). The rate of water mass transformation in the Atlantic Ocean's interior shows that there is a robust buoyancy increase in the North Atlantic Deep Water (NADW, neutral density  $\gamma^n \approx 27.6$ –28.15), with a diapycnal circulation of 0.5–8 Sv between 48°N and 32°S in the Atlantic Ocean. Moreover, tracers within the southward-flowing NADW may undergo a substantial diapycnal transfer, equivalent to a vertical displacement of hundreds of meters in the vertical. This result, confirmed with a zonally averaged numerical model of the AMOC, indicates that mixing can alter where tracers upwell in the Southern Ocean, ultimately affecting their global pathways and ventilation timescales. These results point to the need for a realistic mixing representation in climate models in order to understand and credibly project the ongoing climate change.

**Plain Language Summary** The Atlantic Ocean meridional overturning circulation plays a key role in regulating the global heat and carbon budgets by inter-hemispheric transport of anthropogenic and natural tracers as well as water masses. While most of this transport occurs along nearly horizontal density surfaces in the ocean interior, vertical transport across density levels is key to bringing deep waters back to the surface. Such cross-density transport is facilitated mainly by the internal waves breaking into turbulence and near boundary processes. This work employs a host of observation-based estimates of turbulence in the Atlantic Ocean to (a) better quantify the contribution of cross-density mixing to the inter-hemispheric Atlantic circulation, and (b) discuss the potential implications for pathways and residence times of tracers carried from the North Atlantic to the Southern Ocean. This work calls for a more careful representation of turbulence-induced vertical mixing within the Atlantic Ocean in climate models to better understand and project the ongoing climate change.

## 1. Introduction

The Atlantic Meridional Overturning Circulation (AMOC) constitutes a key component of the global ocean circulation, and plays a central role in the regulation, variability and anthropogenic change of our climate. The AMOC is the primary contributor to the redistribution of heat in the Atlantic Ocean, transporting heat northward in both hemispheres (Forget & Ferreira, 2019). Further, it exerts a profound influence on the sequestration of tracers, such as oxygen and anthropogenic carbon, that are taken up in the process of dense water formation (Gruber et al., 2019).

The AMOC is an overturning cell, encompassing net southward transport of dense waters and net northward return of lighter waters (Figure 1a). The dense southward-flowing waters are produced through surface transformation of lighter waters in the sub-polar North Atlantic, and are additionally sourced by entrainment of Mediterranean Water, and by diapycnal exchanges with northward-flowing intermediate and abyssal waters (Reid, 1994; Talley, 1996). Together, these diverse sources give rise to North Atlantic Deep Water (NADW), which flows

**Funding acquisition:** Ali Mashayek

**Investigation:** Laura Cimoli, Ali Mashayek

**Methodology:** Laura Cimoli, Ali Mashayek

**Resources:** Ali Mashayek

**Supervision:** Helen L. Johnson, David P. Marshall

**Visualization:** Laura Cimoli

**Writing – original draft:** Laura Cimoli, Ali Mashayek

**Writing – review & editing:** Laura Cimoli, Ali Mashayek, Helen L. Johnson, David P. Marshall, Alberto C. Naveira Garabato, Caitlin B. Whalen, Clément Vic, Casimir de Lavergne, Matthew H. Alford, Jennifer A. MacKinnon, Lynne D. Talley

southward at a depth of  $\sim 1,000$ – $4,000$  m and surfaces in the Southern Ocean (Figure 1). Inverse models and ocean state estimates (e.g., Forget et al., 2015; Ganachaud, 2003; Lumpkin & Speer, 2007; Talley, 2013; Talley et al., 2003), as well as direct measurements (e.g., the RAPID-MOCHA array—Cunningham et al., 2007; McCarthy et al., 2015; Srokosz & Bryden, 2015), suggest that the maximum southward transport of the AMOC is around 16–24 Sv (where  $1 \text{ Sv} = 10^6 \text{ m}^3 \text{ s}^{-1}$ ), as shown in Figure 1a from the Estimating the Circulation and Climate of the Ocean (ECCO) state estimate. Underlying the AMOC cell is a weaker overturning cell, in which abyssal Antarctic Bottom Water (AABW) flows northward after sinking to the seafloor around Antarctica (Figure 1a).

NADW is often conceptualized as an adiabatic flow, that is, directed along density surfaces (isopycnals; see neutral density contours in Figure 1a), between the North Atlantic and the Southern Ocean, where density surfaces outcrop (Cessi, 2019; Marshall & Speer, 2012). Several studies, in particular stemming from theoretical investigations or idealized numerical simulations, have suggested that NADW returns to the surface mainly via wind-driven upwelling along the steeply sloping isopycnals outcropping in the Southern Ocean, without any significant role for diapycnal mixing (e.g., Gnanadesikan, 1999; Johnson et al., 2019; Marshall & Speer, 2012; Toggweiler & Samuels, 1998; Wolfe & Cessi, 2011).

However, observation-based inverse models (e.g., Lumpkin & Speer, 2007; Talley et al., 2003) and the ECCO state estimate (Cessi, 2019; Forget et al., 2015) show a reduction in AMOC's transport by about 2–10 Sv between  $24^\circ\text{N}$  and  $32^\circ\text{S}$ , largely driven by downward diffusion of low-latitude surface heat gain (Talley, 2013). An important further contribution to such reduction may be effected by diapycnal mixing near the Atlantic's topographic boundaries, along which a substantial fraction of the AMOC transport occurs (de Lavergne et al., 2022). Several recent investigations of the connection between diapycnal mixing and the turbulent transformation of water masses, especially in regions of topographically enhanced turbulence, have hypothesized that diapycnal mixing induces diapycnal downwelling (i.e., a densification of water masses) in the ocean interior, and diapycnal upwelling (i.e., a lightening of water masses) in the proximity of topographic boundaries (de Lavergne, Madec, Sommer, et al., 2016; Ferrari et al., 2016; Mashayek, Salehipour, et al., 2017; McDougall & Ferrari, 2017). Globally integrated, these transformations have been proposed to result in a net dense-to-light water mass conversion of abyssal waters. The implications of this emerging paradigm for the AMOC's rate and structure are not yet clear.

Importantly, the diapycnal transfer of water masses (i.e., of mass) does not generally explain how tracers (such as anthropogenic carbon, oxygen or nutrients) are redistributed across different water masses by diapycnal mixing. This is because the tracer evolution will also depend on a diffusive diapycnal tracer transport, occurring without a diapycnal mass transfer (Groeskamp et al., 2019). If tracers mix within NADW or with surrounding layers, they may outcrop in substantially different regions and dynamical regimes of the Southern Ocean, and join distinct downstream branches of the overturning circulation. For example, the transport analysis by Lumpkin and Speer (2007) indicates that the neutral density (Jackett & McDougall, 1997) surface  $\gamma^n = 27.6$  roughly separates lighter and denser NADW components with different fates. The former NADW class transforms into lighter waters and returns to the North Atlantic on decadal-to-centennial timescales, whereas the latter class ( $\gamma^n > 27.6$ ) transforms into AABW near Antarctica and re-emerges only on millennial time scales (Lumpkin & Speer, 2007; Naveira-Garabato et al., 2014; Santoso et al., 2006; Sloyan & Rintoul, 2001).

To illustrate the importance of the AMOC in regulating tracer distributions, Figure 1b shows the depth-integrated concentration of anthropogenic carbon from an observational climatology (GLObal Ocean Data Analysis Project, GLODAP; Lauvset et al. (2016)). The formation and southward flow of NADW is reflected in the deeper and faster penetration of anthropogenic carbon in the Atlantic Ocean, where the areal storage is nearly double that in the Pacific Ocean, where there is no deep-water formation (Gruber et al., 2019).

In this study, we investigate the significance of diapycnal mixing for the AMOC and for the transfer of tracers between the AMOC's different water masses, with a focus on the southward-flowing NADW. We employ observation-based, basin-wide estimates of diapycnal mixing, comprising of: (a) direct measurements of the rate of dissipation of turbulent kinetic energy (hereafter dissipation rate) by microstructure probes (Waterhouse et al., 2014); (b) internal wave dissipation rate estimates from strain-based parameterizations (M. Gregg & Kunze, 1991; M. C. Gregg et al., 2003; Kunze et al., 2006; Polzin et al., 2014; Wijesekera et al., 1993) applied to either Argo float measurements (Whalen et al., 2012, 2015) or hydrographic sections (Kunze, 2017b); (c) an energy-constrained, observationally tested parameterization of internal tide-induced dissipation rate (de Lavergne et al., 2020); and (d) a bulk estimate of the water mass transformation rates from an inverse model (Lumpkin

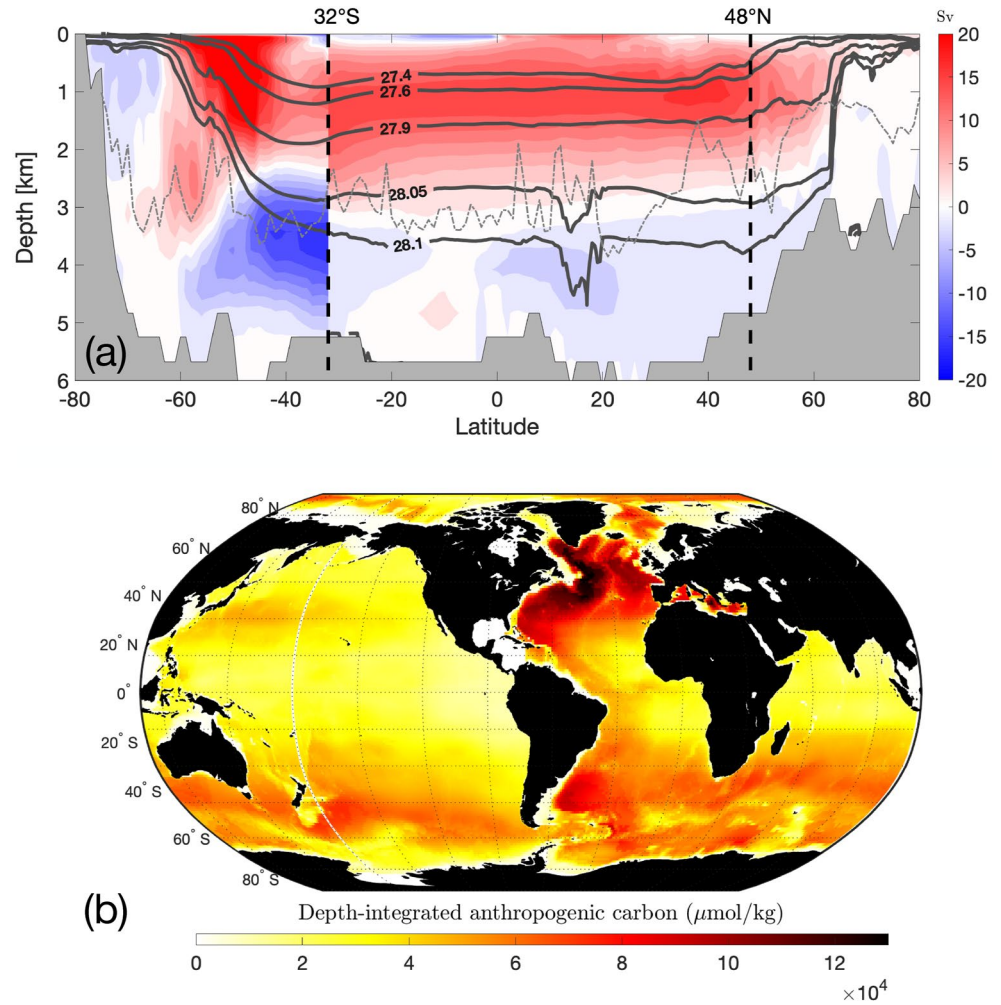


**Figure 1.** (a) Overturning streamfunction from ECCO ocean state estimate (Forget et al., 2015), calculated for the Atlantic Ocean only between 80°N and 32°S, and globally in the Southern Ocean between 32°S and 80°S (hence the discontinuity at 32°S). The maximum transport of the Atlantic Meridional Overturning Circulation is 17 Sv. Contours are every 2 Sv. The thick black lines denote the zonally averaged neutral density levels, calculated from the World Ocean Circulation Experiment climatology (Gouretski and Koltermann (2004). The dashed gray line indicates the average depth of the crest of the Mid-Atlantic Ridge. (b) The depth-integrated concentration of anthropogenic carbon from GLobal Ocean Data Analysis Project climatology (Lauvset et al., 2016).

& Speer, 2007). These estimates have significant uncertainties, some intrinsic to the parameterizations used to infer mixing rates (b, c), and others due to sampling limitations (a, b, d). However, the combination of different approaches enables a comprehensive look at the Atlantic-wide patterns of diapycnal mixing and their implications for ocean circulation and tracer distributions.

## 2. Diapycnal Mixing Estimates in the Atlantic Ocean

Diapycnal mixing in the ocean interior is mainly generated by breaking internal waves, and is typically quantified by relating the rate at which turbulent kinetic energy is dissipated during wave breaking events,  $\epsilon$ , to a turbulent diffusivity coefficient,  $\kappa$ . Diapycnal mixing contributes to the irreversible transformation of a water parcel's density. Defining buoyancy as  $b = -(g/\rho_0)(\rho - \rho_0)$ , where  $\rho_0$  is a reference density, and  $N^2 = \partial^2 b / \partial z^2$  as the buoyancy frequency squared, the buoyancy flux can be approximated, following Osborn (1980), as

$$\mathcal{M} \approx -\kappa N^2 \approx \Gamma \epsilon, \quad (1)$$

which indicates that the buoyancy flux,  $\mathcal{M}$ , is a fraction of the rate at which energy is lost to viscous dissipation,  $\epsilon$ . This fraction is expressed by the turbulent flux coefficient  $\Gamma$ , which here we take to be a constant value



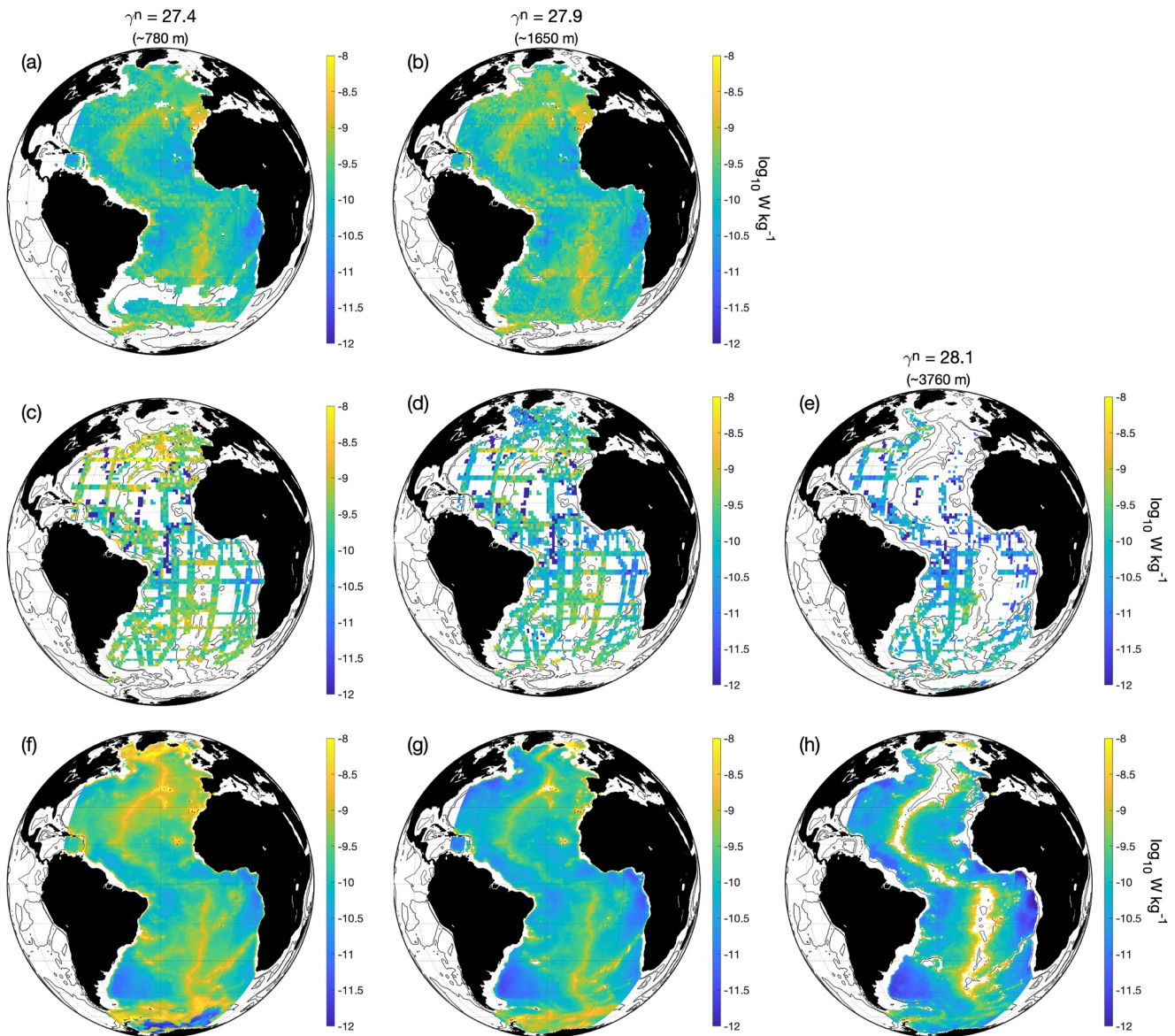


**Figure 2.** Rate of dissipation of turbulent kinetic energy  $\epsilon$  estimated from (a and b) Argo float data (extending work of Whalen et al. (2015)), (c–e) CTD and microstructure data (based on Kunze (2017b) and (Waterhouse et al., 2014)), and (f–h) internal tides (from de Lavergne et al. (2020)), shown on the density surfaces  $\gamma^n = 27.4$  (left column),  $\gamma^n = 27.9$  (middle column), and  $\gamma^n = 28.1$  (right column). The average depth of the density surfaces in the Atlantic Ocean is also shown.

of 0.2, as it is pertinent to shear-driven turbulence and commonly assumed in physical oceanography (e.g., M. Gregg et al. (2018) and Caulfield (2020)). While  $\Gamma$  can be spatially variable (Bouffard & Boegman, 2013; Cimoli et al., 2019; de Lavergne, Madec, Le Sommer et al., 2016; Mashayek & Peltier, 2013; Mashayek, Salehipour, et al., 2017; Mashayek et al., 2022; Spingys et al., 2021), the implications of such variability for mixing are still not well understood on basin scales.

The turbulence estimates collated here are either  $\epsilon$  or  $\kappa$ , from which we infer the buoyancy flux across different neutral density surfaces (Equation 1). The four estimates we use are:

1. *Argo-based* estimates of  $\epsilon$  from a strain-based parameterization applied to Argo float hydrographic data (an updated version of the data set used in Whalen et al. (2012) and Whalen et al. (2015) with higher spatio-temporal resolution). Figures 2a and 2b show the localized estimates of dissipation rate on two different density surfaces, both lying at depths shallower than 2,000 m, where Argo data stops. Available estimates have been interpolated to avoid gaps in areas where Argo data are unavailable in sufficient density. The

Argo-based dissipation estimates display marked spatial variability, with intense dissipation in regions of rough topography, elevated tidal and wind energy inputs, or high eddy kinetic energy (Whalen et al., 2012). Regionally averaged strain-based estimates of  $\epsilon$  agree with similarly averaged microstructure within a factor of 2–3 with no systematic bias (Whalen et al., 2015), therefore the basin-wide averages presented here will have less uncertainty.

2. *CTD plus microstructure* estimates of  $\epsilon$  from a strain-based parameterization applied to CTD (Conductivity, Temperature, and Depth) hydrographic profiles from Kunze (2017a); Kunze (2017b), combined with the dissipation rate directly measured by microstructure profilers from Vic et al. (2019), and gridded on a  $1^\circ$  horizontal grid (Figures 2c–2e). These estimates agree with the Argo-based data (Figures 2a and 2b), both qualitatively, identifying the regions of enhanced turbulence (e.g., in the northwest Atlantic Ocean, an area of enhanced eddy activity, and where the Mid-Atlantic Ridge reaches shallow depths) and weak turbulence (e.g., in the Angola basin); and quantitatively, returning the same magnitude of  $\epsilon$  (with a few exceptions in the mid-Atlantic). Hydrographic and microstructure data have the advantage of providing continuous estimates throughout the full water column based on observations. For example, Figure 2e shows  $\epsilon$  on the neutral density surface  $\sigma_\theta = 28.1$ , where Argo-based estimates are unavailable. Finescale parameterizations can underestimate high dissipation values over rough topography (de Lavergne et al., 2020), and return an overall decrease of  $\epsilon$  with depth, suggesting that most of the turbulent kinetic energy is dissipated in pycnocline waters (Kunze (2017b); Figures 2a–2e).
3. *Tide-generated* estimates of  $\epsilon$  from de Lavergne et al. (2020), which take into account both the contributions of locally breaking (high-mode) and long-distance propagating (low-mode) internal tides. This data set is constructed by accounting for four different dissipative processes (wave-wave interactions, scattering by abyssal hills, dissipation over critical slopes, and shoaling), as well as the waves' horizontal and vertical propagation. de Lavergne et al. (2020) compared this estimate with the dissipation measured by microstructure profilers and parameterized from Argo float data, showing an overall good agreement as discernible in Figures 2f–2h. We will refer to this estimate as “tidally driven” mixing, although in the calculation of the buoyancy flux we also take into account the contribution of geothermal heating from Davies and Davies (2010).
4. *Bulk estimate from an inverse model*. The estimates of turbulence outlined above suffer from two substantial limitations: they lack full spatial coverage (across the globe, in depth and especially close to ocean boundaries), and/or depend on a range of underlying assumptions. As such, it is important to assess inferences from these estimates against bulk diagnostics of basin-scale diapycnal mixing. Here, we consider the inverse estimate from Lumpkin and Speer (2007), which stems from combining hydrographic sections and observation-based datasets of air-sea exchanges of heat and freshwater to quantify the global meridional overturning circulation. They divided the ocean into boxes bounded by hydrographic sections, and inferred the net diapycnal water mass transformation rates (to be defined in Equation 3), from which they inferred turbulent fluxes and basin-averaged turbulent diffusivity  $\kappa$  (see Figure 4 in Lumpkin and Speer (2007)). Such bulk estimates do not provide any information on the spatial pattern of mixing within the large region contained by a box, nor on the processes that underpin the mixing. Processes that cannot be estimated from other observations, and may thus be missing from the first three estimates, are implicitly included in the bulk estimates.

Note that estimate does not account for the dissipation associated with lee waves excited through interaction of geostrophic motions with rough topography. In ocean basins north of the Southern Ocean, the lee wave contribution is modest compared to that of internal tides (Nikurashin & Ferrari, 2011; Waterman et al., 2014). Also unaccounted for is the contribution of the wind-induced near-inertial shear in the upper ocean, as  $\sim 70\%$  of the wind energy is dissipated in the top 200 m (Zhai et al., 2009). The total near-inertial wind power that makes it to the deep ocean is a small fraction of the tidal power (M. H. Alford, 2020).

In the next section we will construct rates of basin-wide diapycnal transformation in the Atlantic Ocean, based on the four datasets mentioned above. We will employ climatological density stratification from the World Ocean Circulation Experiment (WOCE; Gouretski & Koltermann, 2004) for all products to facilitate comparison of the results. Thus, we will not consider temporal variability in mixing.

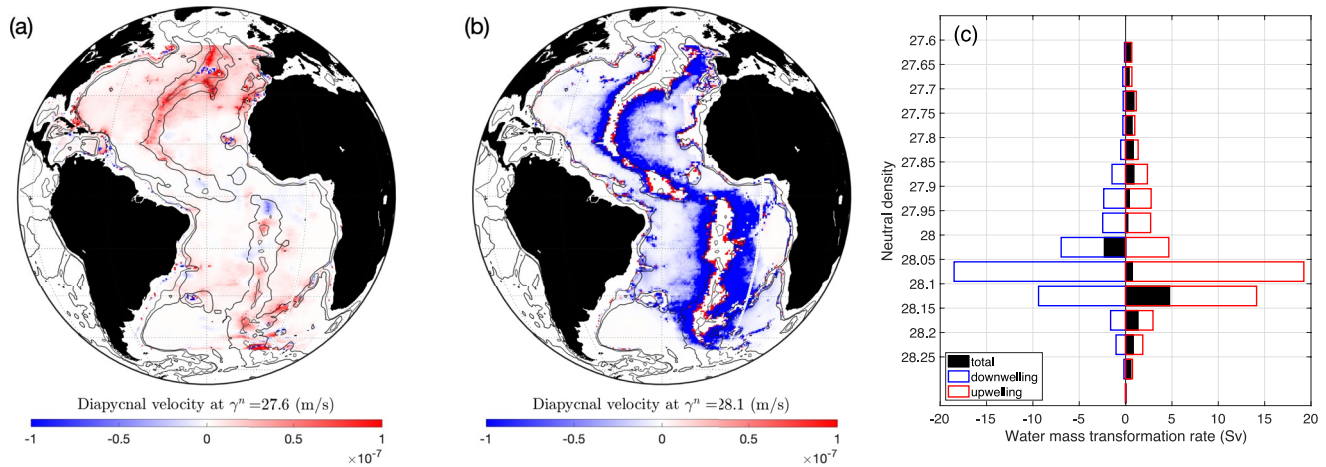


**Figure 3.** (a and b) Diapycnal velocity (Equation 2) calculated from the tidally driven mixing estimate on the neutral density surfaces  $\gamma^n = 27.6$  (a) and  $\gamma^n = 28.1$  (b). Positive values (red) indicate diapycnal upwelling, and negative values (blue) indicate diapycnal downwelling. The 3,000 and 4,000 m isobaths are also shown (thin black lines). (c) Water mass transformation rate (Equation 3) for the tidally driven mixing estimate across the density surfaces bounding the North Atlantic Deep Water flow ( $\gamma^n = 27.6$ –28.15). For each density surface, the total upwelling and downwelling are shown by the empty red and blue bars, respectively, while their residual is shown by the filled black bar. Positive transformation corresponds to a decrease in density.

### 3. Results

#### 3.1. Diapycnal Circulation and Water Mass Transformation Rates Across AMOC Density Levels

Internal wave-driven turbulence can lead to the irreversible transformation of water masses, which may become either lighter or denser. The sign and the rate of the water mass transformation depend on the diapycnal divergence of the buoyancy flux: water masses are transformed only if mixing is vertically non-homogeneous, that is, if there is a diffusive convergence or divergence of buoyancy. Water (mass) moves across density surfaces at the diapycnal velocity (Ferrari et al., 2016):

$$w^* = \frac{\partial_z \mathcal{M}}{\partial_z b}. \quad (2)$$

The diapycnal velocity is positive, and waters become lighter, when the buoyancy flux arising due to mixing ( $\mathcal{M}$ ) decreases with depth, for example, when there is surface-intensified mixing, or in the bottom boundary layer where  $\mathcal{M} \rightarrow 0$  toward the ocean floor (de Lavergne, Madec, Sommer, et al., 2016; Ferrari et al., 2016). In calculating the buoyancy flux divergence at the bottom, a geothermal heat flux is included following Adcroft et al. (2001) and Mashayek et al. (2013). Conversely, diapycnal velocity is negative, and waters become denser, when mixing intensifies with depth, for example, in the ocean interior near rough topography (de Lavergne, Madec, Sommer, et al., 2016; Ferrari et al., 2016; McDougall & Ferrari, 2017). Note that Equation 2 ignores effects related to the non-linearity of the equation of state: these effects are thought to be of secondary importance at the depths (>1,000 m) and latitudes considered here (de Lavergne, Madec, Sommer, et al., 2016; Klocker & McDougall, 2010).

As an example, diapycnal velocities inferred from the estimates of tidally driven diapycnal mixing are shown on the density surfaces  $\gamma^n = 27.6$  and  $\gamma^n = 28.1$  (Figures 3a and 3b). Diapycnal upwelling (red) occurs in the upper ocean, where most of the energy is dissipated (de Lavergne et al., 2020; Kunze, 2017b), and along sloping topography in the bottom boundary layer (de Lavergne, Madec, Sommer, et al., 2016; Ferrari et al., 2016; McDougall & Ferrari, 2017). Diapycnal downwelling (blue) takes place mainly in the deep ocean interior, where the buoyancy flux increases toward the bottom over rough topography, in agreement with microstructure measurements (St Laurent et al., 2001).

The water mass transformation rate across a neutral density surface  $\gamma^n_*$  in the ocean interior is given by the integral of the diapycnal velocity over that density surface:

$$D(\gamma^n_*) = - \iint_{A(\gamma^n_*)} w^* \cdot \hat{\mathbf{n}} dA \quad (3)$$



where  $\hat{n}$  is the unit vector normal to the density surface,  $A$  is the area of the density surface, and the minus sign is used such that water mass transformation is positive when water goes from denser to lighter (following Ferrari et al. (2016)). The net transformation rate is the residual of complex upwelling and downwelling patterns. In the upper ocean, upwelling occurs over the entire basin and is enhanced above the underlying rough topography (Figure 3a). In the abyssal ocean, the net upwelling is due to a balance between boundary upwelling along topographic slopes that host intense turbulence in weakly stratified bottom boundary layers, and downwelling in the more strongly stratified layers above them (Figure 3b; also see de Lavergne et al., 2017; de Lavergne, Madec, Sommer, et al., 2016). Of the three localized estimates of diapycnal mixing used here, only the estimate of tidally driven mixing allows for a full investigation of the relative abyssal up/downwelling contributions; neither the Argo-based nor the CTD- and microstructure-based estimates have sufficient resolution to adequately capture the water mass transformation along the boundaries.

Figure 3c shows the water mass transformation rate  $D(\gamma^n)$  for the tidally driven mixing estimates, spanning the density levels of the southward-flowing AMOC waters ( $\gamma^n = 27.6\text{--}28.15$ ) and the abyssal waters below ( $\gamma^n > 28.15$ ). Upwelling and downwelling are represented by the red and blue bars, respectively, while the net water mass transformation rate integrated over the entire isopycnal area between  $48^\circ\text{N}$  and  $32^\circ\text{S}$  is denoted by the filled black bars. The net water mass transformation is positive for most of the density surfaces analyzed, indicating a lightening of these water masses. This result is consistent with the findings of de Lavergne, Madec, Sommer, et al. (2016), Ferrari et al. (2016), and Kunze (2017a), and agrees with the notion that diapycnal mixing in the deep ocean acts to raise dense waters back to shallower depths, contributing to the AMOC's closure.

While the net water mass transformation across  $\gamma^n = 28.1$  is about 3 Sv, the red and blue bars in Figure 3c indicate more than 21 and 18 Sv of diapycnal upwelling and downwelling, respectively. Thus, although the net suggests a modest turbulent exchange across these density surfaces, the magnitude and pattern of the two contributions indicate that tracers may experience significant up- or downwelling, depending on their distribution, that is, on the extent to which tracers are stirred laterally, homogenized or transported away from the boundaries, as well as on the spatial configuration of diapycnal upwelling and downwelling. Available tracer observations do not have the spatio-temporal resolution to explore this hypothesis, which has been examined in idealized numerical simulations (Drake et al., 2020; Ferrari et al., 2016; Holmes et al., 2019; Mashayek, Ferrari, et al., 2017; Mashayek et al., 2015).

### 3.2. Estimates of Atlantic-Integrated Mixing

The Atlantic-integrated ( $48^\circ\text{N}\text{--}32^\circ\text{S}$ ) residual water mass transformation rate, based on each of the estimates of diapycnal mixing discussed above, is shown in Figure 4a. The density range identified by the pink band ( $\gamma^n = 27.2\text{--}27.7$ ) indicates the approximate boundary between the net southward and northward flows of the AMOC, which varies with latitude. Following Lumpkin and Speer (2007), southward-flowing AMOC waters are denser than  $\gamma^n \approx 27.7$  in the Northern Hemisphere, but the boundary between net southward/northward flows moves to lighter waters (up to  $\gamma^n \approx 27.2$ ) in the Southern Hemisphere. The boundary between the net deep southward-flowing and the net abyssal northward-flowing waters in the Atlantic Ocean is around  $\gamma^n = 28.15$  (Burke et al., 2015).

The net transformation rate is positive for most density classes shown in Figure 4a, indicating a net diapycnal upwelling, that is, a lightening of deep waters. For waters denser than  $\gamma^n = 27.5$ , the four different estimates show a consistent vertical structure: the transformation rate is largest within the southward NADW flow, particularly in the  $\gamma^n = 27.7\text{--}27.9$  density range, it weakens around  $\gamma^n = 28\text{--}28.05$ , and increases again below  $\gamma^n = 28.1$ . The water mass transformations calculated from different mixing estimates, using data collected via distinct approaches and employing various parameterizations or assumptions, exhibit similar qualitative patterns and give us confidence that we can draw general conclusions on the basin-integrated picture.

The water mass transformation rate estimated from Argo floats (red bars) is the smallest overall, with values up to  $\sim 0.8$  Sv at  $\gamma^n = 27.7\text{--}27.95$ , and weaker values on the other density surfaces. The estimate based on CTD data and microstructure profiles (in yellow) results in transformation rates up to  $\sim 1.2$  Sv within the southward NADW pathway ( $\gamma^n = 27.65\text{--}27.95$ ), and smaller values for both lighter and denser isopycnals. The water mass transformation rate calculated from tidally driven mixing (in green) reaches a maximum of  $\sim 3$  Sv at  $\gamma^n = 28.1$ : this density surface has the largest area of contact with the bottom (de Lavergne et al., 2017), resulting in a

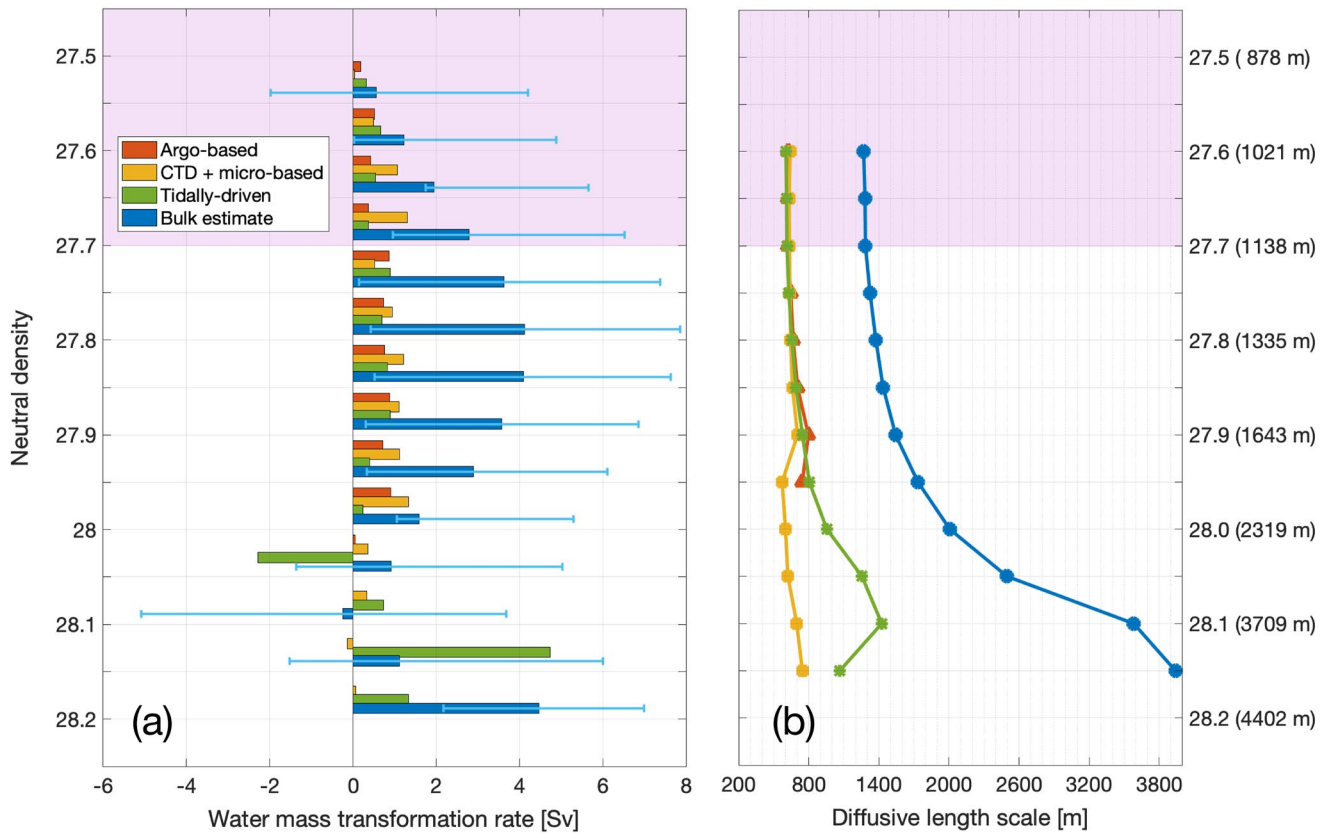


**Figure 4.** (a) Water mass transformation rate (Sv) and (b) vertical diffusive length scale  $L$  (m) calculated from: the Argo-based estimate of diapycnal mixing (red), CTD data + microstructure profile-based estimate (yellow), tidally driven estimate (green), and the inverse model bulk estimate (blue). Errorbars for the inverse model estimate water mass transformation are taken directly from Lumpkin and Speer (2007), where the factors contributing to such uncertainties are discussed in details. The y-axis in panel (b) reports the mean depth of each density surface in the Atlantic Ocean between  $48^\circ\text{N}$  and  $32^\circ\text{S}$ . Pink shading indicates the density range separating the southward and northward flows of the Atlantic Meridional Overturning Circulation (i.e., the layer of near-zero transport). Note that areas with no data in Figure 2 do not contribute to the transformation rates in panel (a).

significant diapycnal transformation of deep waters, in agreement with previous studies (Cimoli et al., 2019; de Lavergne, Madec, Sommer, et al., 2016; de Lavergne et al., 2017; Ferrari et al., 2016; Kunze, 2017b; Mashayek, Salehipour, et al., 2017). The rates of water mass transformation for the tidally driven mixing at lighter density classes are smaller but still substantial. The bulk estimate from Lumpkin and Speer (2007) (in blue) returns the largest transformations, up to  $\sim 4$  Sv at  $\sigma_\theta = 27.8$ – $27.9$ , that is, within the core of the southward NADW flow. However, large uncertainties in the bulk estimate imply that values could be as little as 0.5 Sv or as large as 8 Sv. The abyssal water mass transformation peak at  $\sigma_\theta \sim 28.15$  is suggested to vary within the range  $\sim 2$ – $7$  Sv. We will return to potential reasons for such large uncertainties in the Discussion.

### 3.3. Implications for Diapycnal Transfers Within the AMOC

Given the amount of mixing found within the NADW layer (Figure 4a), water and tracers carried by the southward-flowing limb of the AMOC could undergo substantial diapycnal transfers. To elucidate this possibility, we calculate a diffusive length scale, representing the characteristic vertical distance over which diapycnal mixing can move water and tracers as they are transported in the NADW layer from the North Atlantic ( $48^\circ\text{N}$ ) to the Southern Ocean ( $32^\circ\text{S}$ ). Diffusion across density surfaces depends on the ambient effective turbulent buoyancy flux ( $\mathcal{M}$ ), density stratification ( $N^2$ ) and residence time through the length of the Atlantic ( $\Delta t$ ), taken to be from  $48^\circ\text{N}$  to  $32^\circ\text{S}$  in this calculation.

Following Fick's law of diffusion, the vertical diffusive length scale is



$$\mathcal{L} = 2\sqrt{\kappa\Delta t} = 2\sqrt{\frac{\langle \mathcal{M} \rangle}{\langle N^2 \rangle}} \Delta t, \quad (4)$$

where  $\kappa$  is the basin-average diapycnal diffusivity (used for estimate 4), and  $\langle \mathcal{M} \rangle$  is the basin-average buoyancy flux (used for estimates 1–3 described in Section 2). The average  $N^2$  is calculated from WOCE hydrographic climatology. The residence time  $\Delta t$  is intended to be the average time it takes for a tracer to transit via the AMOC. Such inter-hemispheric transit involves not only north-south transport via the strong western boundary currents but also lateral mixing of tracers between boundary currents, gyres, and equatorial currents, as well as vertical (diapycnal) mixing (Bower et al., 2009; Fine et al., 2002; Holzer & Primeau, 2006; Lozier, 1997; Lozier et al., 2022; MacGilchrist et al., 2017; Rhein et al., 2015).

We estimate the residence time  $\Delta t$  as the ratio of the distance between 48°N and 32°S to the mean southward velocity. The distance is 8,000 km. A mean velocity of  $0.8 \pm 0.2$  cm/s is estimated from the time-average (yr 2004–2010) meridional transport measurements from the RAPID-MOCHA array at 26°N (Moat et al., 2022), for the depth range ~1,000–4,000 m characteristic of the NADW. Assuming that this velocity can be applied at every depth and latitude, which is clearly an oversimplification, the estimated residence time is  $\Delta t$  is ~300 years.

Figure 4b shows the resulting diffusive vertical length scales as a function of density. For mixing estimates (1–3),  $\mathcal{L}$  is between 500 and 1,400 m, while for the bulk inverse estimate (4), it is much larger, between 1,300 and 4,000 m. By construct,  $\mathcal{L}$  is an order-of-magnitude estimate. The large values, especially in the denser waters, imply that mixing is sufficient for tracers to mix across the entire depth range of the southward flowing NADW from the subpolar Atlantic to the Southern Ocean. This further implies the potential mixing of tracers with the upper northward branch of the AMOC or the deeper abyssal circulation. Thus, mixing within the southward flowing limb of the AMOC can significantly alter tracers' global pathways and residence time. Of course, an accurate measure of the integrated effect of mixing on tracer dispersion can only be achieved by consideration of the full range of dynamical processes comprising the AMOC, the spatio-temporal variability of mixing, and the spatial distribution of a given tracer. While we leave such comprehensive analysis to future work, we explore the integrated effect of mixing on tracer dispersion using a simple zonally averaged AMOC framework in the next section.

### 3.4. Diapycnal Tracer Transfers in a Numerical Model

In this section, we use a zonally averaged model of the Atlantic Ocean to show that diapycnal mixing within the AMOC exerts a profound influence on the basin-wide distribution of tracers. Mixing impacts tracer distributions (a) on short time scales by altering the amount of transport across tracer gradients and (b) on long time scales by modifying the ocean circulation and stratification.

We use the zonally averaged model of the Atlantic Ocean by Nikurashin and Vallis (2012) which produces a realistic two-cell AMOC consistent with Figure 1a. Diapycnal mixing is the only component of their original model modified here. Figure 5 shows the overturning streamfunction for two different mixing representations: (a) a constant value of  $\kappa = 3 \times 10^{-5}$  m<sup>2</sup>/s, based on the quasi-constant (in the vertical) diffusivity inferred by Kunze (2017b), and (b) a  $\kappa$  based on the bulk basin-wide estimate of Lumpkin and Speer (2007), hereafter  $\kappa_{L507}$ . The latter overturning streamfunction exhibits a more robust abyssal cell due to enhanced near-bottom mixing. Both simulations' overturning rates agree reasonably well with those based on ECCO (in Figure 1a).

Figure 6 illustrates the time evolution of a passive tracer's concentration for various diapycnal mixing configurations (one configuration per row). To distinguish the short-time scale response of tracer to changes in mixing from the long-term response due to changes in the AMOC (caused by the mixing-induced changes to the AMOC), in some configurations, different diffusivities are used for buoyancy and the passive tracer. For all cases, the simulation is first run until the overturning circulation reaches a steady state. A passive tracer is then injected at the surface in the Northern Hemisphere, with values increasing linearly from 0 at the equator to 1 at the northernmost point. The simulations are continued until the tracer finds its way to the Southern Ocean.

In the first configuration, referred to hereafter as the “control run,” the passive tracer and buoyancy are both subject to a constant modest vertical diffusivity of  $3 \times 10^{-5}$  m<sup>2</sup>/s. The tracer sinks with the deep waters formed at the northern boundary and is advected southward within the NADW. Along the way to the Southern Ocean, a significant portion of the tracer is diffused upward toward lighter northward-flowing waters (note the overturning

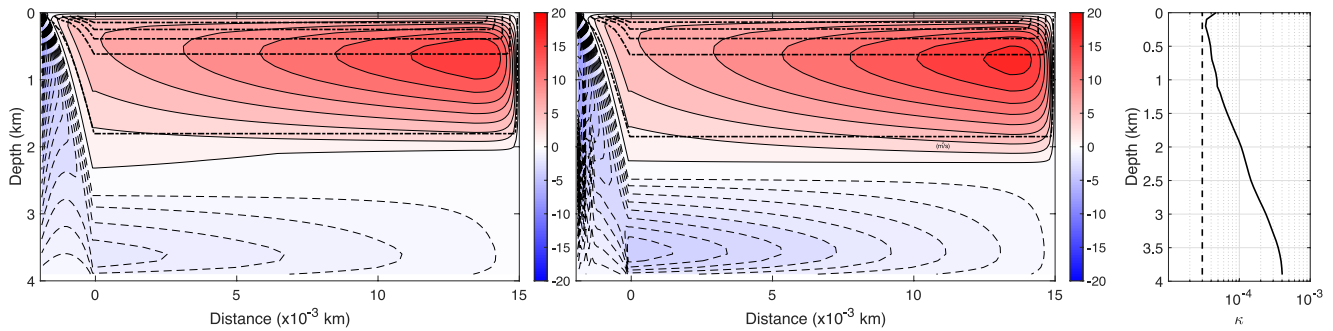


**Figure 5.** Overturning streamfunction in a zonally averaged model of the Atlantic Ocean. The model parameters closely follow those of Nikurashin and Vallis (2012), except for the vertical diffusivity profile. Two cases are considered: the left panel uses a constant vertical diffusivity of  $3 \times 10^{-5} \text{ m}^2/\text{s}$ , chosen from the CTD-based estimate of Kunze (2017b), and the middle panel shows a vertically variable diffusivity based on the bulk estimate of Lumpkin and Speer (2007) (for the Atlantic Ocean), hereafter referred to as  $\kappa_{LS07}$ . The two diffusivities are compared in the right panel.

streamfunction contours in black), and a lesser portion mixes diapycnally with the underlying northward-flowing waters of the lower cell (shown with dashed streamlines).

In a second configuration (second row), enhanced mixing  $\kappa_{LS07}$  is applied only to the tracer while keeping the mixing acting on the buoyancy field constant at the same value as in the control run. Thus, the overturning circulation remains the same as in the control run while the tracer mixing is enhanced. The colored contours show the difference between the tracer concentration in this case and the control run. The net effect of enhanced tracer mixing is an increase in the diapycnal transfer of the tracer toward the abyssal cell, as well as enhanced recirculation of the tracer within the NADW layer. As a result, a lower tracer concentration reaches the Southern Ocean via the southward-flowing NADW.

In a third configuration (third row), we do the opposite perturbation experiment: the tracer is diffused with the constant  $\kappa = 3 \times 10^{-5} \text{ m}^2/\text{s}$  (as in the control run), while the buoyancy field is subject to  $\kappa_{LS07}$ . We let the simulation run forward for this case until a new steady circulation is obtained, then release the tracer. The tracer anomalies naturally reflect the change in circulation: the enhanced mixing strengthens and inflates the abyssal cell

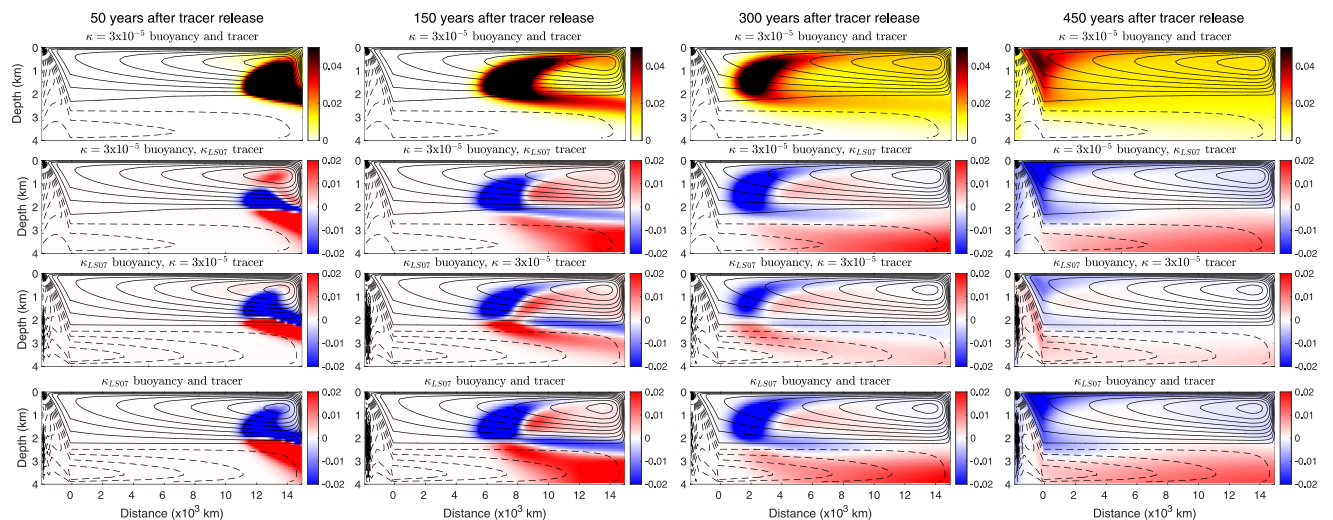


**Figure 6.** Time evolution of a passive tracer in a zonally averaged model of the Atlantic Ocean circulation. The tracer is injected at the surface in the northern hemisphere with values increasing linearly from 0 at the equator to 1 at the northernmost point. Time evolves from left to right, from year 50 after tracer release in the left column to 150, 300, and 450 years in the other columns. The top row shows the tracer concentration when tracer and buoyancy are subject to the same constant diffusivity of  $3 \times 10^{-5} \text{ m}^2/\text{s}$ . Rows 2–4 show perturbation simulations in which either buoyancy, tracer, or both, are subjected to a vertically variable diffusivity based on the Lumpkin and Speer (2007) bulk estimate, with the colors indicating the difference between the tracer concentration for each row and that in the “control” simulation of the top row. In all panels, contours of the meridional overturning streamfunction are shown by solid lines for the Atlantic Meridional Overturning Circulation upper cell and dashed lines for the abyssal cell. The overturnings for rows 1 and 2 are the same as the left panel in Figure 5, and those for rows 3 and 4 are the same as the middle panel in Figure 5.

(as can be seen by comparing the dashed streamlines with those from the top two rows). As a result, more tracer ends up in the lower cell at the expense of the tracer concentration in the upper cell.

Finally, in a fourth configuration (fourth row), both the buoyancy field and the passive tracer are subject to  $\kappa_{LS07}$ . The tracer anomalies, in this case, reflect the combined impacts of mixing-driven changes in the circulation (as in the third row) and changes due to the direct influence of mixing on the tracer (second row). The total effect on timescales of a few centuries is a larger concentration in the abyss and the upper Atlantic, at the expense of mid-depth and Southern Ocean waters.

In summary, Figure 6 makes three important points. First, enhanced diapycnal mixing in the Atlantic Ocean significantly changes the vertical distribution of the tracer by acting on the tracer gradients. Second, enhanced mixing significantly redistributes the tracer in the vertical by changing the underlying, buoyancy-driven circulation. The third point is the existence of two timescales linked to the first two points. Significant spatio-temporal changes in mixing can modify the tracer circulation on timescales that range from a few decades in the upper ocean to millennia in the abyss. Any tracer advected by the circulation will almost immediately “feel” such changes in mixing (similar to row 2) and will additionally be impacted by mixing on a much longer timescale associated with the slow changes in the underlying dynamics (row 3). Here, we apply the same diffusivity profile across the whole model basin. Ellison et al. (2022) showed that even altering the diffusivity profile in the Southern Ocean only can affect the Atlantic redistribution of tracers on the two timescales discussed here.

#### 4. Discussion

We have used a range of observation-based estimates of diapycnal mixing to quantify the role of such mixing within the AMOC, that is, the extent to which water and tracers are transferred diapycnally as they flow from the North Atlantic to the Southern Ocean. Our results indicate that diapycnal mixing contributes modestly to the AMOC's closure: 0.5–8 Sv of NADW upwell diabatically in the ocean interior. While this finding confirms that the AMOC's representation as a mainly adiabatic circulation (commonly assumed by theoretical and numerical modeling works) is reasonable, it also highlights the potential importance of diapycnal mixing for various problems, particularly those involving tracers.

Such importance can be illustrated in two ways. First, we have shown that the residual water mass transformation across any given isopycnal in the deep Atlantic, however small, may stem from potentially much larger individual diapycnal up and downwelling contributions (Figure 3). This suggests that tracer exchanges between density layers may be significantly more vigorous than generally recognized. The covariance between the spatial pattern of mixing and the tracer distribution on any given isopycnal will determine the extent to which mixing redistributes the tracer vertically. This inference points to a critical sampling issue: while data coverage may be adequate to map  $\epsilon$  (see e.g., Kunze, 2017b; Waterhouse et al., 2014; Whalen et al., 2015), our work suggests that limitations associated with the sampling of mixing, especially in the vicinity of topography where upwelling is focused, can make it challenging to characterize the impact of mixing on the vertical transfer of tracers.

Second, setting this mixing-tracer covariance issue aside, an initial estimate of the impact of mixing on tracer transfer has been obtained using a bulk diffusive length scale, which characterizes the vertical distance of mixing-induced tracer transport within the AMOC. This indicates that tracers within the southward-flowing NADW may undergo a substantial diapycnal transfer (equivalent to hundreds of meters in the vertical) to lighter or denser water masses, with potential entrainment into the AMOC's northward branch or, more likely, divergent global pathways and ventilation timescales after upwelling in the Southern Ocean. We highlighted this result with tracer injections in an idealized model of the AMOC. The impact of vertical variations in mixing on tracers was two-fold: first, mixing directly redistributes tracers between different water masses, altering their ventilation pathways and timescales. Second, mixing shapes the basin-scale overturning circulation on centennial-to-millennial timescales, thus indirectly influencing the tracers' global pathways. These two impacts are comparably significant for tracer concentrations but act on different timescales.

Localized and process-based estimates of mixing considered in this study all have significant uncertainties intrinsic to the parameterizations used to infer mixing (de Lavergne et al., 2020; Polzin et al., 2014; Whalen et al., 2015) that are challenging to quantify. Estimates of dissipation rate inferred from Argo floats and CTD profiles depend on choices made in applying the strain-based parameterization, for example, the length of the vertical segments and number of observations selected for averaging, and the shear-to-strain ratio

(Kunze, 2017a, 2017b; Kunze et al., 2006; Whalen et al., 2012, 2015). Here, we averaged the individual estimates over a wide area (the entire Atlantic Ocean), thus mitigating the effect of uncertainties in each estimate (Kunze, 2017a; Whalen et al., 2015). The uncertainty associated with the internal tidal mixing estimate depends on the assumptions about the horizontal and vertical propagation of the low- and high-mode internal tides. The bulk diffusivity estimate relies on the accuracy of the horizontal transports estimated in the inverse model, which themselves depend on uncertainties in the air-sea fluxes used and partially subjective treatment of asynoptic observations. At any rate, although these uncertainties may be of potential significance and motivate further work, the qualitative similarity between the results from the different mixing estimates is encouraging. It suggests that broad patterns of mixing and water mass transformation rates diagnosed here are robust.

The uncertainties listed above may partially explain the large difference between the water mass transformation arising from the localized and tidal estimates and that from the inverse method. However, it is likely that such discrepancy also stems from the inability of Argo float and CTD data to capture turbulent processes in proximity to ocean boundaries and the lack of representation of all boundary processes in the tidally driven mixing estimate employed here. Among such near boundary turbulence hot spots are narrow passages between basins and deep trenches (M. Alford et al., 2013; Van Haren, 2018; Van Haren et al., 2017; Voet et al., 2015), continental slopes (J. D. Nash et al., 2004; J. Nash et al., 2007), mid-ocean ridges (St Laurent et al., 2001; Thurnherr & St. Laurent, 2011), seamounts (Kunze & Toole, 1997; Lueck & Mudge, 1997; Mashayek, Gula, et al., 2021; Toole et al., 1997) and canyons (Carter & Gregg, 2002; Kunze et al., 2012).

Boundary processes, while not included explicitly in the bulk inverse estimate, are implicitly accounted for by this approach, which closes the buoyancy budget of the basin within the constraints imposed by observed hydrographic sections. Our results add to evidence from recent studies in other deep-ocean regions that have also found a discrepancy between bulk estimates of mixing and those based on localized measurements (Huussen et al., 2012; Mashayek, Ferrari, et al., 2017; Voet et al., 2015). Evidence of enhanced mixing in the vicinity of western boundaries in the Atlantic Ocean has been previously reported (Kohler et al., 2014; Stober et al., 2008). Still, the implications for basin-integrated diapycnal upwelling of water masses and tracers have not yet been determined. A further caveat to our results is the omission of variations in the flux coefficient connecting the rates of turbulent energy dissipation and mixing; it is now established that such variations occur and that they can alter the spatial pattern of mixing on basin scales (see de Lavergne, Madec, Le Sommer et al. (2016), Mashayek, Salehipour, et al. (2017), M. Gregg et al. (2018), Cimoli et al. (2019); Mashayek, Caulfield, and Alford (2021), and Mashayek et al. (2022)). Finally, the residence time of tracers, that is, the time a tracer spends over regions with various mixing levels, is next to impossible to measure directly, yet has been suggested to be important in reconciling local and bulk estimates of mixing (Mashayek, Ferrari, et al., 2017).

To conclude, our results suggest that diapycnal mixing within the AMOC, while likely not of leading order importance (yet not insignificant) for the closure of the AMOC, is significant for Atlantic tracer budgets and, by extension, for their global pathways and residence times. This emphasizes the importance of effective parameterization of tracer mixing in ocean/climate models.

## Conflict of Interest

The authors declare no conflicts of interest relevant to this study.

## Data Availability Statement

The CTD-based estimate of diapycnal mixing is available at the repository shared by Kunze (2017b), at <ftp.nwra.com/outgoing/kunze/iwturb>. The internal tide turbulence estimate and the corresponding hydrographic climatology are available at the repository shared by de Lavergne et al. (2020), at <https://www.seanoe.org/data/00619/73082/>. The microstructure data is available at [microstructure.ucsd.edu](http://microstructure.ucsd.edu). The Argo-based turbulence estimate is built from the global Argo float data set [www.argo.net/](http://www.argo.net/) following the methodology describes in Whalen et al. (2012); Whalen et al. (2015). The bulk water mass transformation rate data points in Figure 4 are from Table 2 and Figure 4 of Lumpkin and Speer (2007).



## Acknowledgments

A significant amount of data was assimilated in the mixing estimates that we used in this work, the collection of which took place after years of instrument development and hundreds of at-sea days and would not have been possible without the hard work and skill of the Captain and crew of each research vessel. We thank Rick Lumpkin for providing the estimate of diffusivity in the Atlantic Ocean from his inverse solution. We thank Max Nikurashin for sharing the SAMBUCA code of Nikurashin and Vallis (2012). L.C. thanks support from the Clarendon Scholarship and the U.K. Natural Environment Research Council (NERC) via the D.T.P. in Environmental Research (NE/L002612/1). A.M. acknowledges support from National Environmental Research Council (NE/P018319/1). H.L.J. and D.P.M. acknowledge support from the NERC UK-OSNAP and SNAP-DRAGON Grants (NE/K010948/1, NE/T013494/1). The National Science Foundation OCE-1923558 supported C.B.W. L.D.T. acknowledges NSF OCE-2023545.

## References

- Adcroft, A., Scott, J. R., & Marotzke, J. (2001). Impact of geothermal heating on the global ocean circulation. *Geophysical Research Letters*, 28(9), 1735–1738. <https://doi.org/10.1029/2000gl012182>
- Alford, M., Girtan, J., Voet, G., Carter, G., Mickett, J., & Klymak, J. (2013). Turbulent mixing and hydraulic control of abyssal water in the Samoan passage. *Geophysical Research Letters*, 40(17), 4668–4674. <https://doi.org/10.1002/grl.50684>
- Alford, M. H. (2020). Global calculations of local and remote near-inertial-wave dissipation. *Journal of Physical Oceanography*, 50(11), 3157–3164. <https://doi.org/10.1175/jpo-d-20-0106.1>
- Bouffard, D., & Boegman, L. (2013). A diapycnal diffusivity model for stratified environmental flows. *Dynamics of Atmospheres and Oceans*, 61, 14–34. <https://doi.org/10.1016/j.dynatmoce.2013.02.002>
- Bower, A. S., Lozier, M. S., Gary, S. F., & Böning, C. W. (2009). Interior pathways of the north Atlantic meridional overturning circulation. *Nature*, 459(7244), 243–247. <https://doi.org/10.1038/nature07979>
- Burke, A., Stewart, A. L., Adkins, J. F., Ferrari, R., Jansen, M. F., & Thompson, A. F. (2015). The glacial mid-depth radiocarbon bulge and its implications for the overturning circulation. *Paleoceanography*, 30(7), 1021–1039. <https://doi.org/10.1002/2015pa002778>
- Carter, G. S., & Gregg, M. C. (2002). Intense, variable mixing near the head of Monterey submarine canyon. *Journal of Physical Oceanography*, 32(11), 3145–3165. [https://doi.org/10.1175/1520-0485\(2002\)032<3145:ivmth>2.0.co;2](https://doi.org/10.1175/1520-0485(2002)032<3145:ivmth>2.0.co;2)
- Caulfield, C. (2020). Layering, instabilities, and mixing in turbulent stratified flows. *Annual Review of Fluid Mechanics*, 53(1), 113–145. <https://doi.org/10.1146/annurev-fluid-042320-100458>
- Cessi, P. (2019). The global overturning circulation. *Annual Review of Marine Science*, 11(1), 249–270. <https://doi.org/10.1146/annurev-marine-010318-095241>
- Cimoli, L., Caulfield, C.-C. P., Johnson, H. L., Marshall, D. P., Mashayek, A., Naveira Garabato, A. C., & Vic, C. (2019). Sensitivity of deep Ocean mixing to local internal tide breaking and mixing efficiency. *Geophysical Research Letters*, 43(24), 14622–14633. <https://doi.org/10.1029/2019gl085056>
- Cunningham, S. A., Kanzow, T., Rayner, D., Baringer, M. O., Johns, W. E., Marotzke, J., et al. (2007). Temporal variability of the Atlantic meridional overturning circulation at 26.5°N. *Science*, 317(5840), 935–938. <https://doi.org/10.1126/science.1141304>
- Davies, J., & Davies, D. (2010). Earth's surface heat flux. *Solid Earth*, 1, 5–24. <https://doi.org/10.5194/se-1-5-2010>
- de Lavergne, C., Groeskamp, S., Zika, J., & Johnson, H. L. (2022). The role of mixing in the large-scale ocean circulation. *Ocean Mixing*, 35–63. <https://doi.org/10.1016/b978-0-12-821512-8.00010-4>
- de Lavergne, C., Madec, G., Le Sommer, J., Nurser, A., & Garabato, A. N. (2016). The impact of a variable mixing efficiency on the abyssal overturning. *Journal of Physical Oceanography*, 46(2), 663–681. <https://doi.org/10.1175/jpo-d-14-0259.1>
- de Lavergne, C., Madec, G., Roquet, F., Holmes, R., & McDougall, T. (2017). Abyssal Ocean overturning shaped by seafloor distribution. *Nature*, 551(7679), 181–186. <https://doi.org/10.1038/nature24472>
- de Lavergne, C., Madec, G., Sommer, J. L., Nurser, G., & Garabato, A. N. (2016). On the consumption of Antarctic bottom water in the abyssal ocean. *Journal of Physical Oceanography*, 46(2), 635–661. <https://doi.org/10.1175/jpo-d-14-0201.1>
- de Lavergne, C., Vic, C., Madec, G., Roquet, F., Waterhouse, A. F., Whalen, C., et al. (2020). A parameterization of local and remote tidal mixing. *Journal of Advances in Modeling Earth Systems*, 12(5), e2020MS002065. <https://doi.org/10.1029/2020ms002065>
- Drake, H. F., Ferrari, R., & Callies, J. (2020). Abyssal circulation driven by near-boundary mixing: Water mass transformations and interior stratification. *Journal of Physical Oceanography*, 50(8), 2203–2226. <https://doi.org/10.1175/jpo-d-19-0313.1>
- Ellison, E., Cimoli, L., & Mashayek, A. (2022). Multi-time scale control of Southern Ocean diapycnal mixing over Atlantic tracer budgets. *Climate Dynamics*, 1–2. <https://doi.org/10.1007/s00382-022-06428-5>
- Ferrari, R., Mashayek, A., McDougall, T., Nikurashin, M., & Champin, J.-M. (2016). Turning ocean mixing upside down. *Journal of Physical Oceanography*, 46(7), 2239–2261. <https://doi.org/10.1175/jpo-d-15-0244.1>
- Fine, R. A., Rhein, M., & Andrié, C. (2002). Using a CFC effective age to estimate propagation and storage of climate anomalies in the deep western North Atlantic Ocean. *Geophysical Research Letters*, 29(24), 80–81. <https://doi.org/10.1029/2002gl015618>
- Forget, G., Champin, J.-M., Heimbach, P., Hill, C., Ponte, R., & Wunsch, C. (2015). ECCO version 4: An integrated framework for non-linear inverse modeling and global ocean state estimation. *Geoscientific Model Development*, 8(10), 3071–3104. <https://doi.org/10.5194/gmd-8-3071-2015>
- Forget, G., & Ferreira, D. (2019). Global ocean heat transport dominated by heat export from the tropical Pacific. *Nature Geoscience*, 12(5), 351–354. <https://doi.org/10.1038/s41561-019-0333-7>
- Ganachaud, A. (2003). Large-scale mass transport, water mass formation and diffusivities estimated from world ocean circulation experiment (WOCE) hydrographic data. *Journal of Geophysical Research*, 108(C7), 3213. <https://doi.org/10.1029/2002jc001565>
- Gnanadesikan, A. (1999). A simple predictive model for the structure of the oceanic pycnocline. *Science*, 288(5410), 2077–2079. <https://doi.org/10.1126/science.283.5410.2077>
- Gouretski, V., & Koltermann, K. P. (2004). WOCE global hydrographic climatology. *Berichte des BSH*, 35, 1–52.
- Gregg, M., D'Asaro, E., Riley, J., & Kunze, E. (2018). Mixing efficiency in the ocean. *Annual Review of Marine Science*, 10(1), 443–473. <https://doi.org/10.1146/annurev-marine-121916-063643>
- Gregg, M., & Kunze, E. (1991). Shear and strain in Santa Monica basin. *Journal of Geophysical Research*, 96(C9), 16709–16719. <https://doi.org/10.1029/91jc01385>
- Gregg, M. C., Sanford, T. B., & Winkel, D. P. (2003). Reduced mixing from the breaking of internal waves in equatorial waters. *Nature*, 422(6931), 513–515. <https://doi.org/10.1038/nature01507>
- Groeskamp, S., Griffies, S. M., Iudicone, D., Marsh, R., Nurser, A. G., & Zika, J. D. (2019). The water mass transformation framework for ocean physics and biogeochemistry. *Annual Review of Marine Science*, 11(1), 271–305. <https://doi.org/10.1146/annurev-marine-010318-095421>
- Gruber, N., Clement, D., Carter, B. R., Feely, R. A., Van Heuven, S., Hoppema, M., et al. (2019). The oceanic sink for anthropogenic CO<sub>2</sub> from 1994 to 2007. *Science*, 363(6432), 1193–1199. <https://doi.org/10.1126/science.aau5153>
- Holmes, R. M., de Lavergne, C., & McDougall, T. J. (2019). Tracer transport within abyssal mixing layers. *Journal of Physical Oceanography*, 49(10), 2669–2695. <https://doi.org/10.1175/jpo-d-19-0006.1>
- Holzer, M., & Primeau, F. W. (2006). The diffusive ocean conveyor. *Geophysical Research Letters*, 33(14), L14618. <https://doi.org/10.1029/2006gl026232>
- Huussen, T., Naveira-Garabato, A., Bryden, H., & McDonagh, E. (2012). Is the deep Indian Ocean MOC sustained by breaking internal waves? *Journal of Geophysical Research*, 117(C8), C08024. <https://doi.org/10.1029/2012jc008236>
- Jackett, D., & McDougall, T. (1997). A neutral density variable for the world's oceans. *Journal of Physical Oceanography*, 27(2), 237–263. [https://doi.org/10.1175/1520-0485\(1997\)027<0237:andvft>2.0.co;2](https://doi.org/10.1175/1520-0485(1997)027<0237:andvft>2.0.co;2)

- Johnson, H. L., Cessi, P., Marshall, D. P., Schloesser, F., & Spall, M. A. (2019). Recent contributions of theory to our understanding of the Atlantic meridional overturning circulation. *Journal of Geophysical Research: Oceans*, 124(8), 5376–5399. <https://doi.org/10.1029/2019jc015330>
- Klocker, A., & McDougall, T. J. (2010). Influence of the nonlinear equation of state on global estimates of diapycnal advection and diffusion. *Journal of Physical Oceanography*, 40(8), 1690–1709. <https://doi.org/10.1175/2010jpo4303.1>
- Kohler, J., Mertens, C., Walter, M., Stober, U., Rhein, M., & Kanzow, T. (2014). Variability in the internal wave field induced by the Atlantic deep western boundary current at 16°N. *Journal of Physical Oceanography*, 44(2), 492–516. <https://doi.org/10.1175/jpo-d-13-010.1>
- Kunze, E. (2017a). The internal-wave-driven meridional overturning circulation. *Journal of Physical Oceanography*, 47(11), 2673–2689. <https://doi.org/10.1175/jpo-d-16-0142.1>
- Kunze, E. (2017b). Internal-wave-driven mixing: Global geography and budgets. *Journal of Physical Oceanography*, 47(6), 1325–1345. <https://doi.org/10.1175/jpo-d-16-0141.1>
- Kunze, E., Firing, E., Hummon, J., Chereskin, T., & Thurnherr, A. (2006). Global abyssal mixing inferred from lowered ADCP shear and CTD strain profiles. *Journal of Physical Oceanography*, 36(8), 1553–1576. <https://doi.org/10.1175/jpo2926.1>
- Kunze, E., MacKay, C., McPhee-Shaw, E. E., Morrice, K., Girtin, J. B., & Terker, S. R. (2012). Turbulent mixing and exchange with interior waters on sloping boundaries. *Journal of Physical Oceanography*, 42(6), 910–927. <https://doi.org/10.1175/jpo-d-11-075.1>
- Kunze, E., & Toole, J. M. (1997). Tidally driven vorticity, diurnal shear, and turbulence atop Fieberling Seamount. *Journal of Physical Oceanography*, 27(12), 2663–2693. [https://doi.org/10.1175/1520-0485\(1997\)027<2663:tdvdsa>2.0.co;2](https://doi.org/10.1175/1520-0485(1997)027<2663:tdvdsa>2.0.co;2)
- Lauvset, S. K., Key, R. M., Olsen, A., van Heuven, S., Velo, A., Lin, X., et al. (2016). A new global interior ocean mapped climatology: The 1x1 GLODAP version 2. *Earth System Science Data*, 8, 325–340. <https://doi.org/10.5194/essd-8-325-2016>
- Lozier, M. S. (1997). Evidence for large-scale eddy-driven gyres in the north Atlantic. *Science*, 277(5324), 361–364. <https://doi.org/10.1126/science.277.5324.361>
- Lozier, M. S., Bower, A. S., Furey, H. H., Drouin, K. L., Xu, X., & Zou, S. (2022). Overflow water pathways in the north Atlantic. *Progress in Oceanography*, 208, 102874. <https://doi.org/10.1016/j.pocan.2022.102874>
- Lueck, R. G., & Mudge, T. D. (1997). Topographically induced mixing around a shallow seamount. *Science*, 276(5320), 1831–1833. <https://doi.org/10.1126/science.276.5320.1831>
- Lumpkin, R., & Speer, K. (2007). Global Ocean meridional overturning. *Journal of Physical Oceanography*, 37(10), 2550–2562. <https://doi.org/10.1175/jpo3130.1>
- MacGilchrist, G. A., Marshall, D. P., Johnson, H. L., Lique, C., & Thomas, M. (2017). Characterizing the chaotic nature of ocean ventilation. *Journal of Geophysical Research: Oceans*, 122(9), 7577–7594. <https://doi.org/10.1002/2017jc012875>
- Marshall, J., & Speer, K. (2012). Closure of the meridional overturning circulation through southern ocean upwelling. *Nature Geoscience*, 5(3), 171–180. <https://doi.org/10.1038/ngeo1391>
- Mashayek, A., Cael, B., Cimoli, L., Alford, M., & Caulfield, C. (2022). A physical–statistical recipe for representation of small-scale oceanic turbulent mixing in climate models. *Flow*, 2, E24. <https://doi.org/10.1017/flo.2022.16>
- Mashayek, A., Caulfield, C., & Alford, M. (2021). Goldilocks mixing in oceanic shear-induced turbulent overturns. *Journal of Fluid Mechanics*, 928, A1. <https://doi.org/10.1017/jfm.2021.740>
- Mashayek, A., Caulfield, C., & Peltier, W. (2013). Time dependent, non-monotonic mixing in stratified turbulent shear flows: Implications for oceanographic estimates of buoyancy flux. *Journal of Fluid Mechanics*, 736, 570–593. <https://doi.org/10.1017/jfm.2013.551>
- Mashayek, A., Ferrari, R., Merrifield, S., Ledwell, J., St Laurent, L., & Naveira-Garabato, A. (2017). Topographic enhancement of vertical turbulent mixing in the southern ocean. *Nature Communications*, 8(1), 14197. <https://doi.org/10.1038/ncomms14197>
- Mashayek, A., Ferrari, R. M., & Peltier, W. (2015). Influence of enhanced abyssal diapycnal mixing on stratification and the ocean overturning circulation. *Journal of Physical Oceanography*, 45(10), 2580–2597. <https://doi.org/10.1175/jpo-d-15-0039.1>
- Mashayek, A., Gula, J., Baker, L., Garabato, A. N., Cimoli, L., & Riley, J. (2021). Mountains to climb: On the role of seamounts in upwelling of deep ocean waters.
- Mashayek, A., & Peltier, W. (2013). Shear induced mixing in geophysical flows: Does the route to turbulence matter to its efficiency? *Journal of Fluid Mechanics*, 725, 216–261. <https://doi.org/10.1017/jfm.2013.176>
- Mashayek, A., Salehipour, H., Bouffard, D., Caulfield, C., Ferrari, R., Nikurashin, M., et al. (2017). Efficiency of turbulent mixing in the abyssal ocean circulation. *Geophysical Research Letters*, 44(12), 6296–6306. <https://doi.org/10.1002/2016gl072452>
- McCarthy, G., Smeed, D., Johns, W. E., Frajka-Williams, E., Moat, B., Rayner, D., et al. (2015). Measuring the Atlantic meridional overturning circulation at 26°N. *Progress in Oceanography*, 130, 91–111. <https://doi.org/10.1016/j.pocan.2014.10.006>
- McDougall, T., & Ferrari, R. (2017). Abyssal upwelling and downwelling driven by near-boundary mixing. *Journal of Physical Oceanography*, 47(2), 261–283. <https://doi.org/10.1175/JPO-D-16-0082.1>
- Moat, B., Frajka-Williams, E., Smeed, D., Rayner, D., Johns, W., Baringer, M., et al. (2022). Atlantic meridional overturning circulation observed by the RAPID-MOCHA-WBTS (RAPID-meridional overturning circulation and heatflux array-western boundary time series) array at 26°N from 2004 to 2020 (v2020.2). British Oceanographic Data Centre—Natural Environment Research Council. <https://doi.org/10.5285/e91b10af-6f0a-7fa7-e053-6c86abc05a09>
- Nash, J., Alford, M., Kunze, E., Martini, K., & Kelly, S. (2007). Hotspots of deep ocean mixing on the Oregon continental slope. *Geophysical Research Letters*, 34(1), L01605. <https://doi.org/10.1029/2006gl028170>
- Nash, J. D., Kunze, E., Toole, J. M., & Schmitt, R. W. (2004). Internal tide reflection and turbulent mixing on the continental slope. *Journal of Physical Oceanography*, 34(5), 1117–1134. [https://doi.org/10.1175/1520-0485\(2004\)034<1117:itratm>2.0.co;2](https://doi.org/10.1175/1520-0485(2004)034<1117:itratm>2.0.co;2)
- Naveira-Garabato, A., Williams, A., & Bacon, S. (2014). The three-dimensional overturning circulation of the southern ocean during the WOCE era. *Progress in Oceanography*, 120, 41–78. <https://doi.org/10.1016/j.pocan.2013.07.018>
- Nikurashin, M., & Ferrari, R. (2011). Global energy conversion rate from geostrophic flows into internal lee waves in the deep ocean. *Geophysical Research Letters*, 38(8), L08610. <https://doi.org/10.1029/2011gl046576>
- Nikurashin, M., & Vallis, G. (2012). A theory of the interhemispheric meridional overturning circulation and associated stratification. *Journal of Physical Oceanography*, 42(10), 1652–1667. <https://doi.org/10.1175/jpo-d-11-0189.1>
- Osborn, T. (1980). Estimates of the local-rate of vertical diffusion from dissipation measurements. *Journal of Physical Oceanography*, 10(1), 83–89. [https://doi.org/10.1175/1520-0485\(1980\)010<0083:eotlro>2.0.co;2](https://doi.org/10.1175/1520-0485(1980)010<0083:eotlro>2.0.co;2)
- Polzin, K., Naveira-Garabato, A., Huussen, T., Sloyan, B., & Waterman, S. (2014). Finescale parameterizations of turbulent dissipation. *Journal of Geophysical Research: Oceans*, 119(2), 1383–1419. <https://doi.org/10.1002/2013jc008979>
- Reid, J. L. (1994). On the total geostrophic circulation of the North Atlantic Ocean: Flow patterns, tracers, and transports. *Progress in Oceanography*, 33(1), 1–92. [https://doi.org/10.1016/0079-6611\(94\)90014-0](https://doi.org/10.1016/0079-6611(94)90014-0)
- Rhein, M., Kieke, D., & Steinfeldt, R. (2015). Advection of North Atlantic deep water from the Labrador Sea to the southern hemisphere. *Journal of Geophysical Research: Oceans*, 120(4), 2471–2487. <https://doi.org/10.1002/2014jc010605>

- Santoso, A., England, M., & Hirst, A. (2006). Circumpolar deep water circulation and variability in a coupled climate model. *Journal of Physical Oceanography*, 36(8), 1523–1552. <https://doi.org/10.1175/jpo2930.1>
- Sloyan, B., & Rintoul, S. (2001). The southern ocean limb of the global deep overturning circulation. *Journal of Physical Oceanography*, 31(1), 143–173. [https://doi.org/10.1175/1520-0485\(2001\)031<0143:tsolot>2.0.co;2](https://doi.org/10.1175/1520-0485(2001)031<0143:tsolot>2.0.co;2)
- Spingys, C. P., Naveira Garabato, A. C., Legg, S., Polzin, K. L., Abrahamsen, E. P., Buckingham, C. E., et al. (2021). Mixing and transformation in a deep western boundary current: A case study. *Journal of Physical Oceanography*, 51(4), 1205–1222. <https://doi.org/10.1175/jpo-d-20-0132.1>
- Srokosz, M., & Bryden, H. (2015). Observing the Atlantic meridional overturning circulation yields a decade of inevitable surprises. *Science*, 348(6241), 1255575. <https://doi.org/10.1126/science.1255575>
- St Laurent, L., Toole, J. M., & Schmitt, R. W. (2001). Buoyancy forcing by turbulence above rough topography in the abyssal Brazil basin. *Journal of Physical Oceanography*, 31(12), 3476–3495. [https://doi.org/10.1175/1520-0485\(2001\)031<3476:bfbtar>2.0.co;2](https://doi.org/10.1175/1520-0485(2001)031<3476:bfbtar>2.0.co;2)
- Stober, U., Walter, M., Mertens, C., & Rhein, M. (2008). Mixing estimates from hydrographic measurements in the deep western boundary current of the north Atlantic. *Deep Sea Research Part I: Oceanographic Research Papers*, 55(6), 721–736. <https://doi.org/10.1016/j.dsr.2008.03.006>
- Talley, L. D. (1996). North Atlantic circulation and variability, reviewed for the CNLS conference. *Physica D: Nonlinear Phenomena*, 98(2–4), 625–646. [https://doi.org/10.1016/0167-2789\(96\)00123-6](https://doi.org/10.1016/0167-2789(96)00123-6)
- Talley, L. D. (2013). Closure of the global overturning circulation through the Indian, Pacific, and southern oceans. *Oceanography*, 26(1), 80–97. <https://doi.org/10.5670/oceanog.2013.07>
- Talley, L. D., Reid, J. L., & Robbins, P. E. (2003). Data-based meridional overturning streamfunctions for the global ocean. *Journal of Climate*, 16(19), 3213–3226. [https://doi.org/10.1175/1520-0442\(2003\)016<3213:dmosft>2.0.co;2](https://doi.org/10.1175/1520-0442(2003)016<3213:dmosft>2.0.co;2)
- Thurnherr, A. M., & St. Laurent, L. C. (2011). Turbulence and diapycnal mixing over the east Pacific rise crest near 10°N. *Geophysical Research Letters*, 38(15), L15613. <https://doi.org/10.1029/2011gl048207>
- Toggweiler, J., & Samuels, B. (1998). On the ocean's large-scale circulation near the limit of no vertical mixing. *Journal of Physical Oceanography*, 28(9), 1832–1852. [https://doi.org/10.1175/1520-0485\(1998\)028<1832:otosls>2.0.co;2](https://doi.org/10.1175/1520-0485(1998)028<1832:otosls>2.0.co;2)
- Toole, J. M., Schmitt, R. W., Polzin, K. L., & Kunze, E. (1997). Near-boundary mixing above the flanks of a midlatitude seamount. *Journal of Geophysical Research*, 102(C1), 947–959. <https://doi.org/10.1029/96jc03160>
- Van Haren, H. (2018). High-resolution observations of internal wave turbulence in the deep ocean. In M. Velarde, R. Tarakanov, & A. Marchenko (Eds.), *Springer oceanography, The Ocean in motion*. Springer.
- Van Haren, H., Berndt, C., & Klauke, I. (2017). Ocean mixing in deep-sea trenches: New insights from the challenger deep, Mariana trench. *Deep-Sea Research*, 129, 1–9. <https://doi.org/10.1016/j.dsr.2017.09.003>
- Vic, C., Garabato, A. C. N., Green, J. M., Waterhouse, A. F., Zhao, Z., Melet, A., et al. (2019). Deep-ocean mixing driven by small-scale internal tides. *Nature Communications*, 10(1), 2099. <https://doi.org/10.1038/s41467-019-10149-5>
- Voet, G., Girton, G., Alford, M., Carter, G., Klymak, J., & Mickett, J. (2015). Pathways, volume transport, and mixing of abyssal water in the Samoan passage. *Journal of Physical Oceanography*, 45(2), 562–588. <https://doi.org/10.1175/jpo-d-14-0096.1>
- Waterhouse, A., MacKinnon, J., Nash, J., Alford, M., Kunze, E., Simmons, H., et al. (2014). Global patterns of diapycnal mixing from measurements of the turbulent dissipation rate. *Journal of Physical Oceanography*, 44(7), 1854–1872. <https://doi.org/10.1175/jpo-d-13-0104.1>
- Waterman, S., Polzin, K. L., Naveira Garabato, A. C., Sheen, K. L., & Forryan, A. (2014). Suppression of internal wave breaking in the Antarctic circumpolar current near topography. *Journal of Physical Oceanography*, 44(5), 1466–1492. <https://doi.org/10.1175/jpo-d-12-0154.1>
- Whalen, C., MacKinnon, J., Talley, L., & Waterhouse, A. (2015). Estimating the mean diapycnal mixing using a finescale strain parameterization. *Journal of Physical Oceanography*, 45(4), 1174–1188. <https://doi.org/10.1175/jpo-d-14-0167.1>
- Whalen, C., Talley, L., & MacKinnon, J. (2012). Spatial and temporal variability of global ocean mixing inferred from Argo profiles. *Geophysical Research Letters*, 39(18), L18612. <https://doi.org/10.1029/2012GL053196>
- Wijesekera, H., Padman, L., Dillon, T., Levine, M., Paulson, C., & Pinkel, R. (1993). The application of internal-wave dissipation models to a region of strong mixing. *Journal of Physical Oceanography*, 23(2), 269–286. [https://doi.org/10.1175/1520-0485\(1993\)023<0269:taoiwd>2.0.co;2](https://doi.org/10.1175/1520-0485(1993)023<0269:taoiwd>2.0.co;2)
- Wolfe, C., & Cessi, P. (2011). The adiabatic pole-to-pole overturning circulation. *Journal of Physical Oceanography*, 41(9), 1795–1810. <https://doi.org/10.1175/2011jpo4570.1>
- Zhai, X., Greatbatch, R. J., Eden, C., & Hibiya, T. (2009). On the loss of wind-induced near-inertial energy to turbulent mixing in the upper ocean. *Journal of Physical Oceanography*, 39(11), 3040–3045. <https://doi.org/10.1175/2009jpo4259.1>